

## Atomic properties of $\text{Lu}^+$

Eduardo Paez,<sup>1,2</sup> K. J. Arnold,<sup>1,2</sup> Elnur Hajiyev,<sup>1,2</sup> S. G. Porsev,<sup>3,4</sup>  
V. A. Dzuba,<sup>5</sup> U. I. Safronova,<sup>6</sup> M. S. Safronova,<sup>3,7</sup> and M. D. Barrett<sup>1,2,\*</sup>

<sup>1</sup>Center for Quantum Technologies, 3 Science Drive 2, Singapore 117543

<sup>2</sup>Department of Physics, National University of Singapore, 2 Science Drive 3, Singapore 117551

<sup>3</sup>Department of Physics and Astronomy, University of Delaware, Newark, Delaware 19716, USA

<sup>4</sup>Petersburg Nuclear Physics Institute, Gatchina, Leningrad District 188300, Russia

<sup>5</sup>School of Physics, University of New South Wales, Sydney 2052, Australia

<sup>6</sup>Physics Department, University of Nevada, Reno, Nevada 89557, USA

<sup>7</sup>Joint Quantum Institute, National Institute of Standards and Technology and the University of Maryland, College Park, Maryland 20742, USA

(Received 17 February 2016; published 18 April 2016)

Singly ionized lutetium has recently been suggested as a potential clock candidate. Here we report a joint experimental and theoretical investigation of  $\text{Lu}^+$ . Measurements relevant to practical clock operation are made and compared to atomic structure calculations. Calculations of scalar and tensor polarizabilities for clock states over a range of wavelengths are also given. These results will be useful for future work with this clock candidate.

DOI: [10.1103/PhysRevA.93.042112](https://doi.org/10.1103/PhysRevA.93.042112)

### I. INTRODUCTION

The development of atomic clocks has played an important role in today's society with applications in many different technologies, most notably the Global Positioning System and navigation. Increased levels of performance have allowed tests of fundamental physics [1] and new avenues of exploration in quantum many-body physics [2,3]. Increasing levels of accuracy and stability continue to be made with atomic clocks based on optical transitions in isolated atoms [4–12]. By now a number of groups have demonstrated superior performance over the current cesium frequency standards with the best clocks to date having inaccuracy at the  $1 \times 10^{-18}$  level [4,5,13]. For ion-based clocks, a significant bottleneck to improved levels of accuracy is the relatively low stability achieved with a single ion. Recently singly ionized lutetium has been proposed as a possible candidate to overcome this hurdle [14,15].

The clock transition in singly ionized lutetium is a highly forbidden  $M1$   $^1S_0$ -to- $^3D_1$  transition [14,16]. This ion has a number of fortuitous properties that are almost ideally suited for clock applications [14,15]. The 2.45-MHz linewidth of the  $^3D_1$ -to- $^3P_0^o$  detection transition provides the possibility of a very low Doppler cooling limit and yet is sufficiently large for practical detection. A novel averaging scheme eliminates shifts associated with the  $J = 1$  level placing it on an equal footing with  $J = 0$  to  $J = 0$  candidates [14]. A very large hyperfine and fine structure splitting results in a very low magnetic field dependence of both the average frequency and the component transitions contributing to the average. Finally, initial estimates of the differential scalar polarizability indicate that it is sufficiently small to allow practical room-temperature operation, with a sign that allows micromotion shifts to be eliminated. This latter property has kindled the idea of clock operation on large ion crystals [15].

All of the available low-lying  $D$  states in  $\text{Lu}^+$  are potentially long lived. These spectator states could in principle be used as clock states themselves. However, insofar as clock operation with the  $^3D_1$  state is concerned, the remaining  $D$  levels

could potentially complicate clock operation via the need for a more complicated laser system. In this paper we give a detailed investigation of these potential issues using  $^{175}\text{Lu}^+$ . Measurements of lifetimes and branching ratios relevant to practical clock operation are made and compared to atomic structure calculations. In addition we provide calculations of scalar and tensor polarizabilities for clock states over a range of wavelengths. This work provides the first step in evaluating the potential of this clock candidate and the calculations given will provide a useful reference for future experimental work.

### II. EXPERIMENT SETUP

#### A. Apparatus

The experiments are performed in a four-rod linear Paul trap with axial end caps, similar to the ones described in Refs. [17,18]. The trap consists of four stainless steel rods of diameter 1.0 mm whose centers are arranged on the vertices of a square with 3.6-mm-length sides. A 3.6-MHz rf potential is applied via a step-up transformer to two diagonally opposing electrodes. A small dc voltage applied to the other two electrodes ensures a splitting of the transverse trapping frequencies. Axial confinement is provided by two axial pins separated by 7 mm. Using this configuration, the measured trapping frequencies are  $(\omega_x, \omega_y, \omega_z)/2\pi \approx (350, 300, 80)$  kHz. These frequencies were measured using  $^{138}\text{Ba}^+$ , which is used throughout for continuous sympathetic cooling.

The level structure for  $\text{Lu}^+$  is given in Fig. 1 showing the  $^1S_0$ -to- $^3D_1$  clock transition, and the  $^3D_1$ -to- $^3P_0^o$  transition for detection and cooling. Optical pumping and state preparation are achieved via the  $^3P_1^o$  level. The experiments reported here use  $^{175}\text{Lu}^+$ , which has a nuclear spin  $I = 7/2$ . The 350-nm laser is a frequency-doubled diode and addresses the transition from  $^1S_0$   $F = 7/2$  to  $^3P_1^o$   $F' = 7/2$ . It propagates orthogonal to a 0.5-mT  $B$  field and is linearly polarized along the direction of the field. The measured optical pumping time out of the  $^1S_0$  level is 2  $\mu\text{s}$ , which is the  $1/e$  decay time of the  $^1S_0$  population. The 598-nm laser is also a frequency-doubled diode laser and addresses the transition from  $^3D_1$   $F = 9/2$  to  $^3P_1^o$   $F' = 9/2$ . Optical pumping out of the  $^3D_1$  level is achieved

\*phybmd@nus.edu.sg

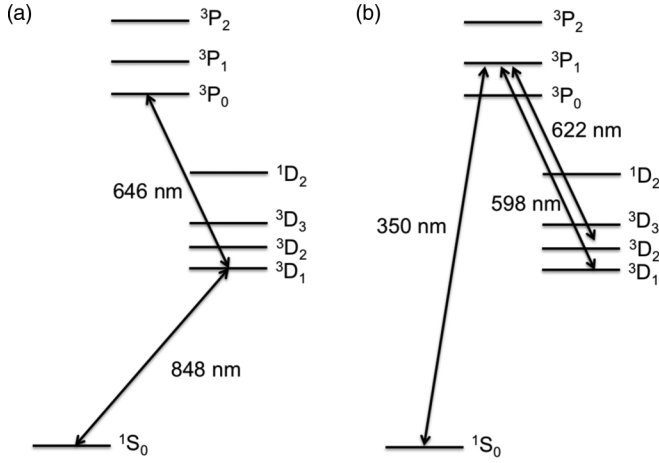


FIG. 1. Lu<sup>+</sup> level structure showing (a) the 848-nm clock and 646-nm detection transitions and (b) the repumping lasers used to optically pump into and out of the <sup>3</sup>D<sub>1</sub> level.

in conjunction with the 646-nm laser and the measured optical pumping time is 6  $\mu$ s. The 622-nm laser is a multimode laser which is sufficiently broad to address all hyperfine states of the <sup>3</sup>D<sub>2</sub>-to-<sup>3</sup>P<sub>1</sub> transition and the measured optical pumping time is 10  $\mu$ s. Both the 598- and 622-nm laser are linearly polarized and propagate along the *B* field.

### B. Detection

As shown in Fig. 1, detection is achieved via scattering on the <sup>3</sup>D<sub>1</sub> to <sup>3</sup>P<sub>0</sub> levels. To address the three separate hyperfine levels, a wideband electro-optic modulator (EOM) generates sidebands of approximately 8 GHz which are separated from the carrier using a cavity. The carrier is frequency shifted via an acousto-optic modulator (AOM) before being recombined with the sidebands. This provides independent frequency control of all three beams. All beams are linearly polarized and propagate along the 0.5-mT *B* field.

Fluorescence at 646 nm is collected onto an avalanche photodiode (APD). A narrow-band filter eliminates scattered light from all other light sources including the 650-nm light used for cooling <sup>138</sup>Ba<sup>+</sup>. This allows continuous sympathetic cooling throughout the <sup>175</sup>Lu<sup>+</sup> detection window. Since the ion is continuously cooled, we can operate at near full saturation for optimum detection efficiency and we typically achieve a mean photon count rate of  $\gtrsim 5$  photons/ms.

For the experiments reported here, we desire a detection scheme to determine when the ion goes bright (dark) with high detection efficiency. To do this we use a Bayesian detection scheme similar to that reported in Ref. [19]. From the number of photons collected in a given detection time step, we update the probability that the ion is in a bright state via

$$P(b|n) = \frac{P(n|b)P(b)}{P(n|b)P(b) + P(n|d)P(d)}, \quad (1)$$

where  $P(b|n)$  [ $P(d|n)$ ] is the conditional probability the ion is in a bright (dark) state given  $n$  photons,  $P(n|b)$  [ $P(n|d)$ ] is the conditional probability of getting  $n$  photons given the ion is in a bright (dark) state, and  $P(b)$  [ $P(d)$ ] is the current probability the ion is in the bright (dark) state. The probability  $P(b)$  is

updated in real time via a field programmable gate array with the conditional probabilities  $P(n|b)$  and  $P(n|d)$  stored on a chip. Detection is initiated with  $P(b) = 0.5$  and terminated when  $P(b)$  reaches preprogrammed thresholds for bright and dark states. We note that the performance of this scheme is insensitive to the choice of time step.

When continuously monitoring for a state change,  $P(b)$  is initialized to 0.5 and updated in subsequent detection windows to  $P(b|n)$  according to Eq. (1). If  $P(b)$  falls below (above) 0.5, the ion is assumed to have gone dark (bright) and detection continues until the appropriate threshold is reached, in which case the state change is deemed verified. Alternatively, if  $P(b)$  subsequently falls above (below) 0.5, the state change is deemed in error, and  $P(b)$  is reinitialized to 0.5. The error rate for determining the ion is in the bright state is limited by hyperfine induced decay from <sup>3</sup>P<sub>0</sub> to states other than <sup>3</sup>D<sub>1</sub>. Thus  $P(b)$  cannot achieve values arbitrarily close to one before the ion decays to a dark state. Similarly, determination of the <sup>3</sup>D<sub>2</sub> dark state is limited by possible decay to the <sup>3</sup>D<sub>1</sub> state.

For the experiments reported in Sec. III D, we also require an accurate estimate of the total collection efficiency. This is achieved using <sup>138</sup>Ba<sup>+</sup> by repeated cycles of optical pumping between the *S*<sub>1/2</sub> and *D*<sub>3/2</sub> levels. Optically pumping from *S*<sub>1/2</sub> to *D*<sub>3/2</sub> produces precisely one 650-nm photon. From the photons collected over several million cycles we infer a collection efficiency of 0.00326(2).

## III. MEASUREMENTS

### A. <sup>3</sup>P<sub>0</sub> branching ratios

Optical pumping via the <sup>3</sup>P<sub>1</sub> level results in an undesired population of the <sup>1</sup>D<sub>2</sub> metastable level. The <sup>3</sup>P<sub>0</sub> level decays to <sup>1</sup>S<sub>0</sub>, <sup>3</sup>D<sub>1</sub>, <sup>3</sup>D<sub>2</sub>, and <sup>1</sup>D<sub>2</sub> with respective decay rates  $W_0$ ,  $W_1$ ,  $W_2$ , and  $W_3$  and branching ratios  $B_k = W_k / \sum W_k$ . Since  $\sum B_k = 1$  we need three more equations to uniquely determine  $W_k$ . This is achieved via three separate optical pumping experiments.

We first prepare the ion in <sup>3</sup>D<sub>1</sub> by optically pumping with the 350-, 622-, and 646-nm lasers until the ion is bright. For this step, we set the threshold count rate to a high value to ensure the initial state is bright with high probability. We then optically pump the ion into <sup>1</sup>S<sub>0</sub> (<sup>3</sup>D<sub>2</sub>) using the 646-, 598-, and 622-nm (350-nm) lasers. The ion is then pumped out of the <sup>1</sup>S<sub>0</sub> (<sup>3</sup>D<sub>2</sub>) level using the 350-nm (622-nm) laser and the population,  $P_0$  ( $P_1$ ), in <sup>3</sup>D<sub>1</sub> is measured. Neglecting any decay of population appearing in <sup>1</sup>D<sub>2</sub> we have

$$P_0 = \frac{B_0}{B_0 + B_3} \frac{B_1}{1 - B_0}, \quad P_1 = \frac{B_2}{B_2 + B_3} \frac{B_1}{1 - B_2}. \quad (2)$$

Similarly, optical pumping to <sup>3</sup>D<sub>2</sub>, followed by optical pumping with both the 350- and 622-nm lasers, gives a population,  $P_2$ , in the <sup>3</sup>D<sub>1</sub> level of

$$P_2 = \frac{B_2}{B_2 + B_3} \frac{B_1}{1 - B_0 - B_2}. \quad (3)$$

For each  $P_k$ ,  $2 \times 10^4$  measurements were made giving  $P_0 = 0.3027(32)$ ,  $P_1 = 0.3166(33)$ , and  $P_2 = 0.9669(13)$ . The inferred branching ratios from these measurements are given in Table I along with theoretical estimates from Sec. IV B. The error bars given are the statistical error. The main systematic is due to decay of the <sup>1</sup>D<sub>2</sub> during optical pumping. Since the

TABLE I. Branching ratios for decay from  $^3P_1^o$ . Theoretical values are from calculations given in Sec. IV B.

Lower level	Expt.	Theory
$6s^2\ ^1S_0$	0.3915(44)	0.376
$6s5d\ ^3D_1$	0.1862(17)	0.186
$6s5d\ ^3D_2$	0.4178(45)	0.435
$6s5d\ ^1D_2$	0.00438(18)	0.0036

measured optical pumping time for each laser is  $\sim 10\ \mu\text{s}$ , which is much less than the  $^1D_2$  lifetime as discussed in the next section, the effect of the decay is less than the statistical error.

There is fair agreement between the experimental and theoretical results with the three main decay channels being within 4%. The larger discrepancy of  $\sim 18\%$  for decay to  $^1D_2$  can be expected given the significantly smaller decay rate.

### B. $^1D_2$ Lifetime

To measure the  $^1D_2$  lifetime, we first optically pump to this level using the 350-, 598-, 622-, and 646-nm lasers. After (10 ms), we switch off the 598-nm laser and monitor fluorescence of the 646-nm light. The  $^1D_2$  lifetime is due to an  $E2$  decay to  $^1S_0$ . However, spin mixing gives a small contribution from  $M1$  transitions to  $^3D_2$  as discussed in Sec. IV B and values of relevant transitions are tabulated in Table V. Decay to  $^3D_3$  occurs with a branching ratio  $\sim 1\%$  and the lifetime of this state is  $> 10\ \text{s}$ . Hence, these decays are infrequent and result in very long dark periods. Decay to  $^3D_2$  or  $^1S_0$  occurs with probability  $q_S$ . These levels are optically pumped to the detection level,  $^3D_1$ , with a small probability,  $p_S$ , of being repumped back to  $^1D_2$ . Neglecting effects of decays to  $^3D_3$  and optical pumping times, the distribution of dark times is exponential with a rate  $W_S^{(m)} = (1 - p_S q_S) W_S$ , where  $W_S$  is the total linewidth of the  $^1D_2$  level. In Fig. 2, we give the measured distribution of dark times from which we infer  $W_S^{(m)} = 5.41(12)\ \text{s}^{-1}$ . For these data we have eliminated all times less than 200 ms or greater than 1 s with 200 ms subtracted of the remaining times. Eliminating times less than 200 ms removes any data points resulting from imperfect optical pumping to the  $^1D_2$  level, and eliminating all times

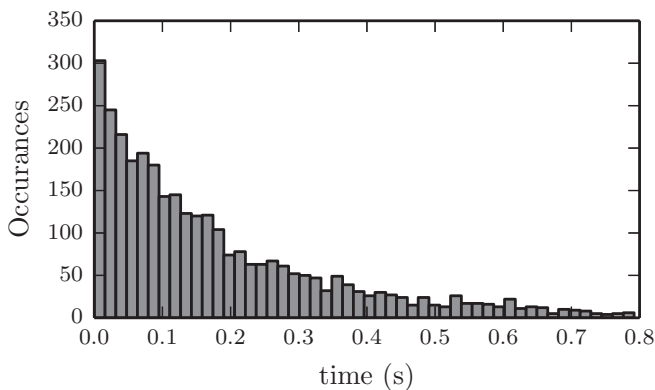


FIG. 2. Histogram of dark times associated with the  $^1D_2$  decay. We have omitted all times less than 200 ms or greater than 1 s with 200 ms subtracted of the remaining times.

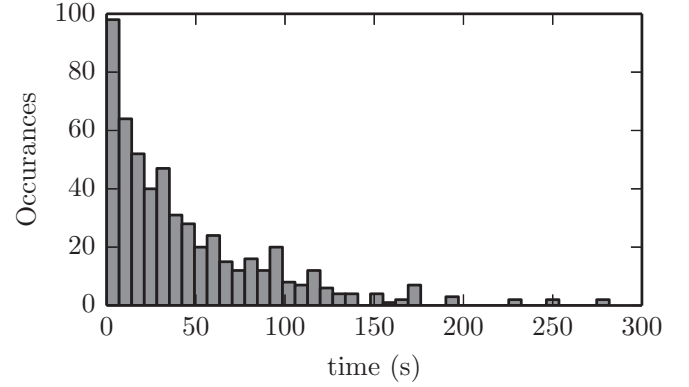


FIG. 3. Histogram of dark times associated with the  $^3D_2$  decay.

greater than 1 s eliminates a small number of events associated with decay into  $^3D_3$ .

Denoting the  $M1$  decay rates from  $^1D_2$  to  $^3D_2$  by  $W_{S,J}$  and the  $E2$  decay rate from  $^1D_2$  to  $^1S_0$  by  $W_{S,0}$ , we can express the total linewidth,  $W_S$ , by

$$W_{S,0} = \frac{W_S^{(m)} - (W_{S,1} + W_{S,3})}{1 - p_S} - W_{S,2}, \quad (4)$$

and

$$W_S = \frac{W_S^{(m)}}{1 - p_S} - \frac{p_S}{1 - p_S} (W_{S,1} + W_{S,3}), \quad (5)$$

where we have used the fact that

$$q_S = \frac{W_{S,0} + W_{S,2}}{W_S}. \quad (6)$$

In terms of the branching ratios,  $B_k$ , from Sec. III A, we have

$$p_S = \frac{B_3}{B_1 + B_3}. \quad (7)$$

This may be determined from the measurements,  $P_k$ , made in Sec. III A and we infer  $p_S = 0.02297(88)$ . From the calculated  $M1$  transition rates given in Table V we infer decay rates  $5.20(12)\ \text{s}^{-1}$  and  $5.53(12)\ \text{s}^{-1}$  for  $W_{S,0}$  and  $W_S$ , respectively. The errors given include only the statistical uncertainty from the experimental measurements. We note that the measured rates are  $\sim 30\%$  larger than the theoretical estimates given in Sec. IV B.

### C. $^3D_2$ Lifetime

We measure the  $^3D_2$  lifetime similarly to the  $^1D_2$  case. We first optically pump to  $^3D_2$  using the 350-, 598-, and 646-nm lasers. After (10 ms), we switch off the 598-nm laser and monitor fluorescence of the 646-nm light. The  $^3D_2$  lifetime is due to a spin-forbidden  $E2$  decay to  $^1S_0$  with a small contribution from an  $M1$  decay to  $^3D_1$ . Decays to  $^1S_0$  result in optical pumping to  $^3D_1$  and repumping to  $^3D_2$ . Neglecting optical pumping times, the distribution of dark times is also exponential with a rate  $W_T^{(m)} = (1 - p_T q_T) W_T$ , where  $p_T$  is the probability of being repumped from  $^1S_0$  to  $^3D_2$  and  $q_T$  is the branching ratio for decay from  $^3D_2$  to  $^1S_0$ . In Fig. 3, we give the measured distribution of dark times from which we infer  $W_T^{(m)} = 0.022(1)\ \text{s}^{-1}$ . Note that, for each dark cycle, optically pumping to  $^3P_1^o$  can result in a population of  $^1D_2$  which extends

the optical pumping time. Since the probability that this occurs is small and the lifetime of this state is much less than the measured mean dark time we may neglect this effect.

We can express the  $E2$  decay rate,  $W_{T,0}$ , and total linewidth  $W_T$  as

$$W_{T,0} = \frac{1}{1 - p_T} (W_T^{(m)} - W_{2,1}) \quad (8)$$

and

$$W_T = \frac{W_T^{(m)}}{1 - p_T} - \frac{p_T}{1 - p_T} W_{2,1}, \quad (9)$$

where  $W_{2,1}$  is the  $M1$  decay rate for the  ${}^3D_2$ -to- ${}^3D_1$  transition and we have used the fact that

$$q_T = \frac{W_{T,0}}{W_T}. \quad (10)$$

In terms of the branching ratios,  $B_k$ , from Sec. III A, we have

$$p_T = \frac{B_2}{1 - B_0}. \quad (11)$$

This may be determined from the measurements,  $P_k$ , made in Sec. III A and we infer  $p_T = 0.6917(33)$ . Together with the calculated  $M1$  transition rates given in Table V we infer decay rates 0.0519(33) and 0.0579(33) for  $W_{T,0}$  and  $W_T$ , respectively. The errors given include only the statistical uncertainty from the experimental measurements. We note that the measured rates are  $\sim 25\%$  larger than the theoretical estimates given in Sec. IV B.

Given that the measured lifetime is very long, measurements could potentially be compromised by off-resonant scattering out of  ${}^3D_2$  by the barium cooling lasers, the 350-nm repump laser or the 646-nm detection beam. Of these, the most significant scattering rate is from coupling to the  $5d5p^3F_2$  level by the 350-nm laser. From dipole matrix elements given in Table II and a measured intensity of  $\sim 500/\text{cm}^2$ , the scattering rate from  ${}^3D_2$  to  ${}^3D_1$  averaged over all possible  ${}^3D_2$  states is  $\sim 3.5 \times 10^{-5} \text{ s}^{-1}$ . This is less than 1% of the calculated  $M1$  decay rate between these states and so contributes much less than the statistical error to the overall decay rates. We can expect scattering rates to  ${}^3D_3$  and  ${}^1D_2$  to be of a similar magnitude and thus equally negligible.

#### D. Hyperfine quenching of ${}^3P_0^o$

Decay from  ${}^3P_0^o$  to  ${}^3D_1$  is the only dipole allowed transition from  ${}^3P_0^o$ . However, the hyperfine interaction induces a low multipole electromagnetic decay to other states. In the case of  $\text{Lu}^+$ , this results in a quenching of the fluorescence rate for the  ${}^3D_1$ -to- ${}^3P_0^o$  detection channel. When fluorescing on this transition, the rate of scattering out of the detection channel is given by

$$\lambda = w\rho_{\text{ec}} = \frac{w}{W} \frac{\langle n \rangle}{q\tau_D}, \quad (12)$$

where  $W$  is the linewidth of the upper state,  $w$  is the total decay rate from  ${}^3P_0^o$  to states other than  ${}^3D_1$ ,  $\langle n \rangle$  is the background subtracted mean number of photons collected in a time  $\tau_D$ , and  $q$  is the overall detection efficiency of the imaging system. Measuring  $\lambda$  involves determining when the ion goes dark and so the measured rate must also include the error

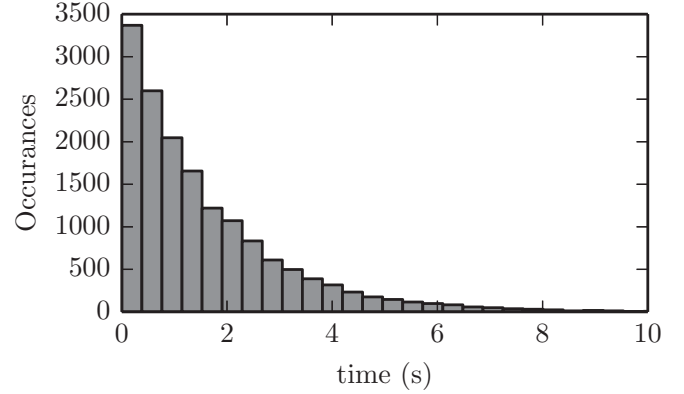


FIG. 4. Histogram of bright times when fluorescing on the  ${}^3D_1$ -to- ${}^3P_0^o$  transition.

rate in that determination. Even an error rate of  $1 \times 10^{-3}$  in a 1-ms detection time would result in a significant contribution to the measured rate. Since there is negligible probability of repumping from the dark state back to the bright state, we can repeatedly test a dark-state event to confirm the measurement similar to the approach reported in Ref. [19].

To measure  $\lambda$ , we first optically pump using 350-, 622-, and 646-nm lasers until the ion is bright. For this step, we set the threshold count rate to a high value to ensure the initial state is bright with high probability. We then switch off the repump lasers and monitor the time the ion remains fluorescent. The distribution of bright times is given in Fig. 4, which gives a fitted value of  $\lambda = 0.624(5)$ . Using measured count rates for the bright and dark states of 6.290(5) and 0.560(3) per millisecond, respectively, together with the measured detection efficiency of 0.00326(2) we infer a ratio  $w/W = 3.55(6) \times 10^{-7}$ . We used an artificial background to match the photon count rate of a bright ion to determine the contribution of the measured rate from detection errors. Out of  $1 \times 10^5$  events we obtained an average detection time of 6 ms with no errors found. This bounds the contribution to  $< 0.0016/\text{s}$ , which is well below the statistical uncertainty.

Decay out of the detection channel is dominated by decays from  ${}^3P_0^o$  to  ${}^1S_0$  and  ${}^3D_2$ . In two separate experiments, we determine the contribution from each of these decays by repumping using either the 350- or the 622-nm laser after the ion is confirmed dark and measure the fraction returning to the bright state. From these measurements and the branching ratios determined in Sec. III A the percentage of decays going to  ${}^1S_0$  and  ${}^3D_2$  are 0.497(19) and 0.562(30), respectively. These values are in reasonable agreement with theoretical values given in Table VIII.

## IV. THEORY

In this section we give details of atomic structure calculations. We start with polarizabilities of relevant clock states, namely the  $6s^2 {}^1S_0$ ,  $5d6s {}^3D_1$ , and  $5d6s {}^3D_2$  levels. We then determine lifetimes and branching ratios for low-lying levels, followed by a determination of the quenching rate of the  ${}^3P_0^o$  level.

### A. Polarizabilities

We evaluated the scalar static and dynamic polarizabilities of the  $6s^2 {}^1S_0$ ,  $5d6s {}^3D_1$ , and  $5d6s {}^3D_2$  states of  $\text{Lu}^+$  using the

TABLE II. Contributions to the  $6s^2\ ^1S_0$ ,  $5d6s\ ^3D_1$ , and  $5d6s\ ^3D_2$  scalar static polarizabilities of Lu<sup>+</sup> in atomic units. The contributions to the valence polarizabilities of several lowest-lying intermediate states are listed separately with the corresponding absolute values of electric-dipole reduced matrix elements given in the column labeled “ $D$ ”. The theoretical and experimental [26] transition energies are given in columns  $\Delta E_{\text{th}}$  and  $\Delta E_{\text{expt}}$ . The remaining valence contributions to the  $^1S_0$  polarizability are given in the row labeled “Other.” For the  $^3D_1$  and  $^3D_2$  polarizabilities we present the contribution of other (not explicitly listed in the table) intermediate states with fixed total angular momentum  $J_n$  in rows labeled “Other ( $J_n = 0, 1, 2, 3$ ).” In rows labeled “Total ( $J_n = 0, 1, 2, 3$ )” we give total contribution of *all* intermediate states with fixed total angular momentum  $J_n$ . In rows “Total val.” we present the total values of  $\alpha_v$ . The contributions from the  $\alpha_c$  and  $\alpha_{vc}$  terms are listed together in rows labeled “Core + Vc.” The dominant contributions to the polarizabilities, listed in columns  $\alpha[A]$  and  $\alpha[B]$ , are calculated with the experimental [26] and theoretical energies, respectively.

State	Contribution	$\Delta E_{\text{th}}$	$\Delta E_{\text{expt}}$	$D^a$	$\alpha[A]$	$\alpha[B]$	
$6s^2\ ^1S_0$	$6s^2\ ^1S_0-6s6p\ ^3P_1^o$	29 073	28 503	0.820	3.45	3.39	
	$6s^2\ ^1S_0-6s6p\ ^1P_1^o$	38 862	38 223	3.518	47.38	46.60	
	$6s^2\ ^1S_0-5d6p\ ^3D_1^o$	46 593	45 532	0.811	2.11	2.07	
	$6s^2\ ^1S_0-5d6p\ ^3P_1^o$	51 285	50 049	0.447	0.59	0.57	
	$6s^2\ ^1S_0-5d6p\ ^1P_1^o$	60 214	59 122	1.354	4.54	4.46	
	Other				2.03	2.03	
	Total val.				60.10	59.11	
	Core + Vc				3.92	3.92	
	Total				64.02	63.03	
	Recommended					63.0	
	$5d6s\ ^3D_1$	$5d6s\ ^3D_1-6s6p\ ^3P_0^o$	15 297	15 468	1.480	6.91	6.99
		$5d6s\ ^3D_1-5d6p\ ^3P_0^o$	38 664	38 167	1.892	4.57	4.52
		Other ( $J_n = 0$ )				0.33	0.33
		Total ( $J_n = 0$ )				11.82	11.83
$5d6s\ ^3D_1-6s6p\ ^3P_1^o$		16 521	16 707	1.287	4.83	4.89	
$5d6s\ ^3D_1-5d6p\ ^3D_1^o$		34 041	33 736	2.391	8.26	8.19	
$5d6s\ ^3D_1-5d6p\ ^3P_1^o$		38 733	38 253	2.089	5.56	5.49	
Other ( $J_n = 1$ )					0.59	0.59	
Total ( $J_n = 1$ )					19.25	19.16	
$5d6s\ ^3D_1-6s6p\ ^3P_2^o$		20 510	20 657	0.351	0.29	0.29	
$5d6s\ ^3D_1-5d6p\ ^3F_2^o$		29 925	29 429	2.741	12.46	12.25	
$5d6s\ ^3D_1-5d6p\ ^1D_2^o$		34 094	33 662	1.716	4.27	4.21	
$5d6s\ ^3D_1-5d6p\ ^3D_2^o$		35 488	35 108	2.259	7.09	7.01	
$5d6s\ ^3D_1-5d6p\ ^3P_2^o$		39 899	39 405	0.555	0.38	0.38	
Other ( $J_n = 2$ )					4.50	4.50	
Total ( $J_n = 2$ )					28.99	28.65	
Total val.					60.05	59.64	
Core + Vc					3.84	3.84	
Total					63.89	63.48	
Recommended					63.5		
$5d6s\ ^3D_2$	$5d6s\ ^3D_2-6s6p\ ^3P_0^o$	15 867	16 068	2.084	7.91	8.01	
	$5d6s\ ^3D_2-6s6p\ ^1P_1^o$	25 656	25 788	0.814	0.75	0.76	
	$5d6s\ ^3D_2-5d6p\ ^3D_1^o$	33 387	33 097	1.986	3.49	3.46	
	Other ( $J_n = 1$ )				5.26	5.26	
	Total ( $J_n = 1$ )				17.41	17.49	
	$5d6s\ ^3D_2-6s6p\ ^3P_2^o$	19 857	20 018	1.220	2.18	2.19	
	$5d6s\ ^3D_2-5d6p\ ^3F_2^o$	29 271	28 790	2.552	6.62	6.51	
	$5d6s\ ^3D_2-5d6p\ ^1D_2^o$	33 440	33 023	0.098	0.01	0.01	
	$5d6s\ ^3D_2-5d6p\ ^3D_2^o$	34 834	34 469	2.653	5.97	5.91	
	Other ( $J_n = 2$ )				3.71	3.71	
	Total ( $J_n = 2$ )				18.49	18.34	
	$5d6s\ ^3D_2-5d6p\ ^3F_3^o$	33 052	32 483	3.727	12.52	12.30	
	$5d6s\ ^3D_2-5d6p\ ^3D_3^o$	36 720	36 298	2.748	6.09	6.02	
	Other ( $J_n = 3$ )				4.13	4.13	
	Total ( $J_n = 3$ )				22.73	22.45	
	Total val.				58.63	58.27	
	Core + Vc				3.84	3.84	
	Total				62.47	62.10	
	Recommended					62.1	

<sup>a</sup>The values are obtained in the CI+all-order approximation and include RPA,  $\sigma$ , SR, and normalization corrections.

high-precision relativistic method that combines configuration interaction (CI) and the linearized coupled-cluster (all-order) method [20]. In this CI+all-order method, the energies and wave functions are determined from the time-independent multiparticle Schrödinger equation

$$H_{\text{eff}}(E_n)\Phi_n = E_n\Phi_n, \quad (13)$$

where the effective Hamiltonian is defined as

$$H_{\text{eff}}(E) = H_{\text{FC}} + \Sigma(E). \quad (14)$$

Here  $H_{\text{FC}}$  is the Hamiltonian in the frozen core approximation and  $\Sigma$  is the energy-dependent correction, which takes into account virtual core excitations in all orders. To establish the importance of the higher-order corrections, we also carried out the calculations constructing the effective Hamiltonian using second-order many-body perturbation theory (CI+MBPT method) [21].

We separate the scalar dynamic polarizability  $\alpha(\omega)$  into three parts:

$$\alpha(\omega) = \alpha_v(\omega) + \alpha_c(\omega) + \alpha_{vc}(\omega), \quad (15)$$

where  $\alpha_v$  is the valence polarizability,  $\alpha_c$  is the ionic core polarizability, and  $\alpha_{vc}$  is a small term that corrects ionic core polarizability for the Pauli-principle-violating excitations to occupied valence shells.

The valence part of the ac electric dipole polarizability of the  $|0\rangle$  state is

$$\begin{aligned} \alpha_v(\omega) &= 2 \sum_k \frac{(E_k - E_0)|\langle\Phi_0|D_0|\Phi_k\rangle|^2}{(E_k - E_0)^2 - \omega^2} \\ &= \sum_k \left[ \frac{|\langle\Phi_0|D_0|\Phi_k\rangle|^2}{E_k - E_0 + \omega} + \frac{|\langle\Phi_0|D_0|\Phi_k\rangle|^2}{E_k - E_0 - \omega} \right], \end{aligned} \quad (16)$$

where  $D_0$  is the  $z$  component of the effective electric dipole operator  $\mathbf{D}$ , defined in atomic units ( $\hbar = m = |e| = 1$ ) as  $\mathbf{D} = -\mathbf{r}$ . The effective (or “dressed”) electric dipole operator includes random-phase approximation (RPA), core-Brueckner ( $\sigma$ ), structural radiation (SR), and normalization corrections which are described in detail in Ref. [22]. In order to accurately account for highly excited discrete states and a continuum we calculated  $\alpha_v(\omega)$  using an inhomogeneous equation in valence space rather than the sum-over-states formula given by Eq. (16). We use the Sternheimer [23] or Dalgarno-Lewis [24] method implemented in the framework of the CI+all-order approach following Ref. [25]. Given the  $\Phi_0$  wave function and energy  $E_0$  of the  $|0\rangle$  state, we find intermediate-state wave functions  $\delta\psi_{\pm}$  from the inhomogeneous equation,

$$\begin{aligned} |\delta\psi_{\pm}\rangle &= \frac{1}{H_{\text{eff}} - E_0 \pm \omega} \sum_k |\Phi_k\rangle \langle\Phi_k|D_0|\Phi_0\rangle \\ &= \frac{1}{H_{\text{eff}} - E_0 \pm \omega} D_0|\Phi_0\rangle. \end{aligned} \quad (17)$$

Using Eq. (16) and  $\delta\psi_{\pm}$  introduced above, we obtain

$$\alpha_v(\omega) = \langle\Phi_0|D_0|\delta\psi_{+}\rangle + \langle\Phi_0|D_0|\delta\psi_{-}\rangle, \quad (18)$$

where superscript  $v$  emphasizes that only excitations of the valence electrons are included in the intermediate-state wave functions  $\delta\psi_{\pm}$  due to the presence of  $H_{\text{eff}}$ .

### 1. Static polarizabilities

In the case of static polarizabilities,  $\omega = 0$ , Eq. (16) is written as

$$\alpha_v(0) = 2 \sum_k \frac{|\langle\Phi_0|D_0|\Phi_k\rangle|^2}{E_k - E_0}. \quad (19)$$

While we do not use the sum-over-states approach in the calculation of the polarizabilities, it is important to establish the dominant contributions to the final values for the purpose of estimating theoretical uncertainties. We combine the electric-dipole matrix elements and energies according to the sum-over-states formula, Eq. (19), for the valence polarizability to calculate the contributions of specific transitions between low-lying states, and these are given in Table II. Remaining valence contributions of higher-lying states are given in rows labeled “Other.”

We have carried out two calculations of the dominant contributions of the intermediate states to the polarizabilities. In the first calculation (column  $\alpha$  [B] in Table II) we used our theoretical values of the energy levels in the denominator of Eq. (19). In the second calculation (column  $\alpha$  [A] in Table II) we used experimental energies, where available. Corresponding theoretical and experimental [26] transition energies are given in columns  $\Delta E_{\text{th}}$  and  $\Delta E_{\text{expt}}$  in  $\text{cm}^{-1}$ . The difference between the results is  $-1.6\%$  for the  $^1S_0$  polarizability and  $-0.6\%$  for the  $^3D_1$  and  $^3D_2$  polarizabilities, demonstrating that deviation of our theoretical energies from the experimental values does not significantly affect the overall accuracy of the polarizabilities. The absolute values of the corresponding reduced electric-dipole matrix elements in atomic units are listed in columns labeled “ $D$ ”. These are calculated using the CI + all-order method and include RPA,  $\sigma$ , SR, and normalization corrections. Calculation of the RPA,  $\sigma$ , and SR corrections is discussed in Ref. [22].

The contributions from  $\alpha_c$  and  $\alpha_{vc}$  terms evaluated in the RPA are listed together in rows labeled “Core + Vc.” Taking into account that the main contribution to the  $^3D_1$  and  $^3D_2$  levels comes from the  $5d_{3/2}6s$  configuration (99% and 80%, respectively), we determined  $\alpha_{vc}$  terms for the  $^3D_{1,2}$  polarizabilities as  $\alpha_{vc}(5d_{3/2}) + \alpha_{vc}(6s)$ . In rows labeled “Total” we present the total values of the scalar static  $^1S_0$ ,  $^3D_1$ , and  $^3D_2$  polarizabilities. Our final values are given in rows labeled “Recommended.”

To determine uncertainties of the polarizabilities we have also calculated them using two other approximations: the CI+MBPT+RPA and CI+all-order+RPA. In both cases only RPA corrections were included. The CI+MBPT method omits higher-order core-valence correlations. The results obtained in the CI+MBPT+RPA, CI+all-order+RPA, and CI+all-order+AC approximations (where abbreviation “AC” means *all corrections*, including RPA,  $\sigma$ , SR, and normalization) are presented in Table III in columns (1), (2), and (3), correspondingly.

We consider the results obtained in the CI+all-order+AC approximation as the final values according to the Sr study [27]. Comparison of the data in columns (2) and (3) in Table III illustrates that the corrections beyond RPA only slightly change the values of the  $^1S_0$  and  $^3D_{1,2}$  polarizabilities.

TABLE III. The scalar ( $\alpha_0$ ) and tensor ( $\alpha_2$ ) polarizabilities, obtained in the CI+MBPT+RPA, CI+all-order+RPA, and CI+all-order+AC approximations (where “AC” means *all corrections*) are presented (in a.u.) in columns (1), (2), and (3), correspondingly. Final (recommended) values are given in the last column. The uncertainties are given in parentheses.

Polarizability	(1)	(2)	(3)	Final
$\alpha_0(6s^2\ ^1S_0)$	62.5	63.3	63.0	63.0(0.8)
$\alpha_0(5d6s\ ^3D_1)$	61.5	64.3	63.5	63.5(2.8)
$\alpha_2(5d6s\ ^3D_1)$	-4.8	-5.2	-5.1	-5.1(4)
$\alpha_0(5d6s\ ^3D_2)$	60.3	62.9	62.1	62.1(2.6)
$\alpha_2(5d6s\ ^3D_2)$	-5.1	-5.7	-5.6	-5.6(6)
$\alpha_0(^3D_1) - \alpha_0(^1S_0)$	-1.0	1.0	0.5	0.5
$\alpha_0(^3D_2) - \alpha_0(^1S_0)$	-2.2	-0.4	-0.9	-0.9

We estimate the polarizability uncertainties as the spread of the results in columns (1)–(3).

## 2. Dynamic polarizabilities

We have also calculated the dynamic scalar and tensor polarizabilities for the  $^1S_0$ ,  $^3D_1$ , and  $^3D_2$  states for the wavelengths of experimental interest. The results, presented in Table IV, are obtained in the framework of the CI+all-order+AC approximation; i.e., all corrections to the matrix elements are included.

In Fig. 5 we plot differential scalar polarizabilities  $\alpha(^3D_1) - \alpha(^1S_0)$  and  $\alpha(^3D_2) - \alpha(^1S_0)$  represented by red solid and blue dashed lines, respectively, vs the wavelength  $\lambda$ . The vertical dotted lines correspond to  $\lambda = 1064$  and  $1560$  nm.

### B. Lifetimes of the low-lying states

In Table V, we list the lifetimes  $\tau$  of the low-lying  $6s6p\ ^3P_J^o$  and  $5d6s\ ^3D_J$  states together with most important reduced matrix elements, and relevant transition rates and branching ratios.

The  $E1$ ,  $E2$ , and  $M1$  transition probabilities (in  $s^{-1}$ ) are obtained in terms of reduced matrix elements (MEs) of the electric-dipole, electric-quadrupole, and magnetic-dipole operators, and transition frequencies  $\omega$  as

$$W_{E1}(\gamma J \rightarrow \gamma' J') = 2.02613 \times 10^{-6} \frac{\omega^3 \langle \gamma' J' || D || \gamma J \rangle^2}{2J+1},$$

TABLE IV. The dynamic scalar ( $\alpha_0$ ), tensor ( $\alpha_2$ ), and differential  $\Delta_{1,2} \equiv \alpha(^3D_{1,2}) - \alpha(^1S_0)$  polarizabilities (in a.u.), obtained in the CI+all-order+AC approximation, are calculated for the wavelengths (frequencies) given in the first (second) row.

$\lambda$ (nm)		847.7	1064	1560	1760	10600
$\omega$ (a.u.)		0.05375	0.04282	0.02921	0.02589	0.00430
$6s^2\ ^1S_0$	$\alpha_0$	68.9	66.6	64.6	64.3	63.0
$5d6s\ ^3D_1$	$\alpha_0$	85.4	73.9	67.6	66.6	63.6
	$\alpha_2$	-13.0	-8.3	-6.2	-5.9	-5.1
$5d6s\ ^3D_2$	$\alpha_0$	79.6	70.9	65.6	64.8	62.2
	$\alpha_2$	-14.1	-9.1	-6.8	-6.5	-5.6
	$\Delta_1$	16.5	7.3	2.9	2.3	0.5
	$\Delta_2$	10.7	4.3	1.0	0.5	-0.9

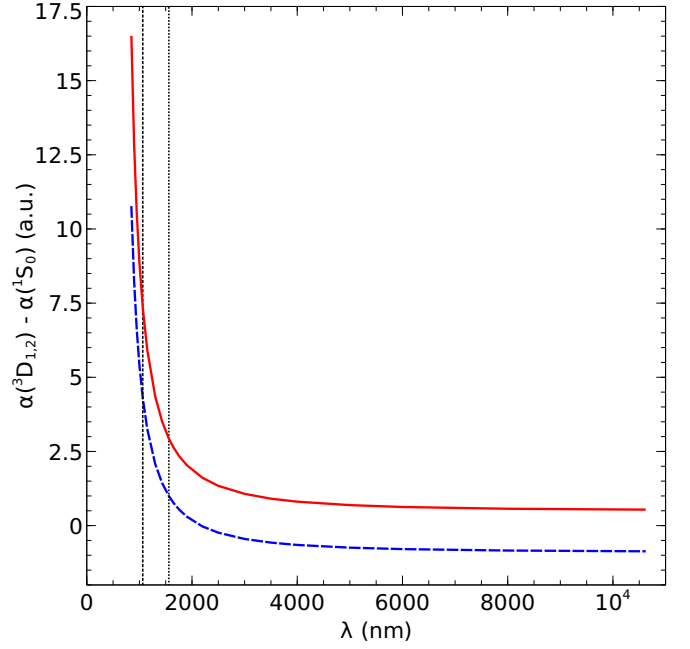


FIG. 5. Differential scalar polarizabilities  $\alpha(^3D_1) - \alpha(^1S_0)$  and  $\alpha(^3D_2) - \alpha(^1S_0)$  represented by red solid and blue dashed lines, respectively, vs the wavelength  $\lambda$ . The vertical dotted lines correspond to  $\lambda = 1064$  and  $1560$  nm.

$$W_{E2}(\gamma J \rightarrow \gamma' J') = 1.11995 \times 10^{-22} \frac{\omega^5 \langle \gamma' J' || Q_E || \gamma J \rangle^2}{2J+1},$$

$$W_{M1}(\gamma J \rightarrow \gamma' J') = 2.69735 \times 10^{-11} \frac{\omega^3 \langle \gamma' J' || \mu || \gamma J \rangle^2}{2J+1}.$$

In these equations, MEs of the  $E1$  and  $E2$  operators are expressed in a.u., MEs of the  $M1$  operator in Bohr magnetons ( $\mu_0$ ), and the decay rates  $\omega$  are expressed in  $cm^{-1}$ .

We determine the lifetimes, listed in the last column of Table V, as  $\tau = 1/W_{\text{tot}}$  with  $W_{\text{tot}} \equiv \sum_k W_k$ , where  $W_k$  are the individual decay rates. The branching ratios,  $B_k$ , are determined as  $B_k = W_k/W_{\text{tot}}$ .

To estimate the uncertainty of theoretical values, we calculate the decay rates

$$\begin{aligned}
 W_0 &\equiv W(6s6p\ ^3P_1^o \rightarrow 6s^2\ ^1S_0), \\
 W_1 &\equiv W(6s6p\ ^3P_1^o \rightarrow 5d6s\ ^3D_1), \\
 W_2 &\equiv W(6s6p\ ^3P_1^o \rightarrow 5d6s\ ^3D_2), \\
 W_3 &\equiv W(6s6p\ ^3P_1^o \rightarrow 5d6s\ ^1D_2), \quad (20)
 \end{aligned}$$

using three different methods: (1) CI+MBPT+RPA, (2) CI+all-order+RPA, and (3) CI+all-order+AC approximations. These results are given in Table VI. The spread of the values calculated in these approximations (1)–(3) gives an estimate of the uncertainties in the final results. Comparing the results obtained in the (2) CI+all-order+RPA and (3) CI+all-order+AC approximations, we find that the corrections beyond RPA play a very insignificant role and we take the results presented in columns labeled (3) as final.

TABLE V. The energies (in  $\text{cm}^{-1}$ ) are counted from the ground  $6s^2 1S_0$  state. The fifth column gives the type of transition. The reduced MEs of  $E1$  and  $E2$  operators (in a.u.) and  $M1$  operator (in  $\mu_0$ ) are presented in sixth column. The individual decay rates,  $W_k$  (in  $\text{s}^{-1}$ ), branching ratios ( $B_k$ ), and lifetimes ( $\tau$ ) are listed in columns 7–9. These quantities are evaluated in the CI+all-order+AC approximation. The numbers in brackets represent powers of 10.

Upper level		Lower level		Transition	ME	$W_k$ $\text{s}^{-1}$	$B_k$	$\tau$
Term	Energy	Term	Energy					
<i>Transitions from the even-parity states</i>								
$6s5d\ ^3D_1$	11 796	$6s^2\ ^1S_0$	0	$M1$	0.0006	5.14[−6]	1.00	1.95[+5] (s)
$6s5d\ ^3D_2$	12 435	$6s^2\ ^1S_0$	0	$E2$	2.509	4.19[−2]	0.88	20.9 (s)
		$6s5d\ ^3D_1$	11 796	$E2$	4.523	4.88[−8]	0.00	
			11 796	$M1$	2.055	5.94[−3]	0.12	
$6s5d\ ^3D_3$	14 199	$6s5d\ ^3D_1$	11 796	$E2$	1.601	3.29[−6]	0.00	10.8 (s)
		$6s5d\ ^3D_2$	12 435	$E2$	4.969	6.74[−6]	0.00	
			12 435	$M1$	2.094	9.27[−2]	1.00	
$6s5d\ ^1D_2$	17 333	$6s^2\ ^1S_0$	0	$E2$	10.63	3.96	0.92	0.23 (s)
		$6s5d\ ^3D_1$	11 796	$E2$	1.018	1.21[−4]	0.00	
			11 796	$M1$	0.524	2.51[−1]	0.06	
		$6s5d\ ^3D_2$	12 435	$E2$	1.319	1.10[−4]	0.00	
			12 435	$M1$	0.218	3.01[−2]	0.01	
		$6s5d\ ^3D_3$	14 199	$E2$	1.327	1.19[−5]	0.00	
			14 199	$M1$	0.531	4.68[−2]	0.01	
<i>Transitions from the odd-parity states</i>								
$6s6p\ ^3P_0^o$	27 264	$5d6s\ ^3D_1$	11 796	$E1$	1.480	1.64[+7]	1.00	61.0 (ns)
$6s6p\ ^3P_1^o$	28 503	$6s^2\ ^1S_0$	0	$E1$	0.820	1.05[+7]	0.38	35.7 (ns)
		$5d6s\ ^3D_1$	11 796	$E1$	1.287	5.22[+6]	0.19	
		$5d6s\ ^3D_2$	12 435	$E1$	2.084	1.22[+7]	0.43	
		$5d6s\ ^1D_2$	17 333	$E1$	0.329	1.00[+5]	<0.01	
$6s6p\ ^3P_2^o$	32 453	$5d6s\ ^3D_1$	11 796	$E1$	0.351	4.40[+5]	0.02	35.8 (ns)
		$5d6s\ ^3D_2$	12 435	$E1$	1.220	4.84[+6]	0.17	
		$5d6s\ ^3D_3$	14 199	$E1$	3.015	2.24[+7]	0.80	
		$5d6s\ ^1D_2$	17 333	$E1$	0.445	2.77[+5]	0.01	
$6s6p\ ^1P_1^o$	38 224	$6s^2\ ^1S_0$	0	$E1$	3.518	4.67[+8]	0.95	20.8 (ns)
		$5d6s\ ^3D_2$	12 435	$E1$	0.814	7.67[+6]	0.02	
		$5d6s\ ^1D_2$	17 333	$E1$	0.994	6.08[+6]	0.01	

### C. Hyperfine quenching of a state with $J = 0$

The hyperfine quenching rate of a state with total angular momentum  $J = 0$  is given by

$$W(\gamma J = 0 \rightarrow \gamma' J') = \frac{4\alpha^3 \omega^3}{3} \frac{1}{(2J+1)(2I+1)} \times \sum_k \frac{\langle I || N^{(k)} || I \rangle^2}{3(2k+1)} |S_k|^2, \quad (21)$$

where  $\omega$  is the ( $\gamma J = 0 \rightarrow \gamma' J'$ ) transition frequency and

$$S_k \equiv \sqrt{\frac{3}{2k+1}} \sum_{\gamma_n} \frac{\langle \gamma' J' || D || \gamma_n J_n \rangle \langle \gamma_n J_n || T^{(k)} || \gamma J = 0 \rangle}{E_n - E_{\gamma J}} + \sum_{\gamma_m J_m \neq \gamma' J'} \frac{\langle \gamma' J' || T^{(k)} || \gamma_m J_m \rangle \langle \gamma_m J_m || D || \gamma J = 0 \rangle}{E_m - E_{\gamma' J'}}, \quad (22)$$

TABLE VI. The decay rates  $W_k$  determined by Eq. (20) (in  $\text{s}^{-1}$ ) and branching ratios, obtained in (1) CI+MBPT+RPA, (2) CI+all-order+RPA, and (3) CI+all-order+AC approximations. The experimental values from Sec. III A are given in the last column. The numbers in brackets represent powers of 10.

	Probabilities				Branching ratios			
	(1)	(2)	(3)		(1)	(2)	(3)	Expt.
$W_0$	1.24[+7]	1.07[+7]	1.05[+7]	$B_0$	0.408	0.375	0.376	0.392
$W_1$	5.33[+6]	5.33[+6]	5.22[+6]	$B_1$	0.176	0.186	0.186	0.186
$W_2$	1.25[+7]	1.25[+7]	1.22[+7]	$B_2$	0.413	0.435	0.434	0.418
$W_3$	9.59[+4]	1.02[+5]	1.00[+5]	$B_3$	0.00316	0.00357	0.00357	0.00436

TABLE VII. The absolute values of MEs of the  $T^{(1)}$  and  $T^{(2)}$  operators (in MHz) obtained in (1) CI+MBPT+RPA, (2) CI+all-order+RPA, and (3) CI+all-order+AC approximations presented in columns labeled (1), (2), and (3), correspondingly. The final values and assigned uncertainties (in parentheses) are given in the last column.

ME	(1)	(2)	(3)	Final
$\langle 6s6p\ ^3P_1^o    T^{(1)}    6s6p\ ^3P_0^o \rangle$	12 427	11 964	10 833	11 960(1000)
$\langle 6s6p\ ^1P_1^o    T^{(1)}    6s6p\ ^3P_0^o \rangle$	4 324	4 352	3 965	4 350(400)
$\langle 5d6s\ ^3D_1    T^{(1)}    5d6s\ ^3D_2 \rangle$	19 465	18 682	16 780	18 680(1900)
$\langle 6s6p\ ^3P_2^o    T^{(2)}    6s6p\ ^3P_0^o \rangle$	1 789	1 780	1 672	1 780(110)
$\langle 5d6s\ ^3D_1    T^{(2)}    5d6s\ ^3D_3 \rangle$	200	198	250	200(50)
$\langle 5d6s\ ^3D_1    T^{(1)}    5d6s\ ^1D_2 \rangle$	10 718	10 618	9 750	10 620(870)
$\langle 5d6s\ ^3D_1    T^{(2)}    5d6s\ ^1D_2 \rangle$	76	70	116	70(45)

where  $Q$ ,  $\mu$ , and  $T^{(k)}$  are defined in the Appendix. The  $^{175}\text{Lu}^+$  ion has the nuclear spin  $I = 7/2$ . Its nuclear magnetic moment  $\mu$ , expressed in nuclear magnetons  $\mu_N$ , is  $\mu/\mu_N = 2.2323(11)$  [28] and the nuclear quadrupole moment is  $Q = 3.49(2)$  b [29].

In Table VII we list absolute values of the reduced matrix elements of  $T^{(1)}$  and  $T^{(2)}$  operators. To illustrate the role of different corrections, we carried out three calculations and found the MEs in (1) CI+MBPT+RPA, (2) CI+all-order+RPA, and (3) CI+all-order+AC approximations. Respective values are listed in the table in columns labeled (1), (2), and (3).

In contrast with the MEs of the electric-dipole operator, the corrections beyond RPA ( $\sigma$ , SR, and normalization) are large for the matrix elements of  $T^{(1)}$  and  $T^{(2)}$  operators. They contribute to large MEs at the level of 10% and even more to smaller MEs. In particular, it was essential to account for the SR corrections for calculating the MEs of the  $T^{(2)}$  operator between  $D_J$  states. The SR contributions are  $\sim 20\%$  to  $\langle 5d6s\ ^3D_1 || T^{(2)} || 5d6s\ ^3D_{2,3} \rangle$  and  $40\%$  to  $\langle 5d6s\ ^3D_1 || T^{(2)} || 5d6s\ ^1D_2 \rangle$ .

We note that while the RPA corrections were calculated to all orders, the corrections beyond RPA were obtained only in the second order of MBPT, which usually overestimates respective contribution. For this reason our final (recommended) values are based on the results obtained in the CI+all-order+RPA approximation while the assigned uncertainties are determined as the differences between the CI+all-order+RPA and CI+all-order+AC values.

We determined the hyperfine quenching rates for the  $6s6p\ ^3P_0^o$  state. We present the results obtained in (1) CI+MBPT+RPA, (2) CI+all-order+RPA, and (3) CI+all-order+AC approximations in Table VIII. The probability of the main E1 ( $6s6p\ ^3P_0^o\ 5d6s\ ^3D_1$ ) transition,  $W^{(0)}$ , is given in the first row. The quenching rates of the  $6s6p\ ^3P_0^o-6s^2\ ^1S_0$ ,  $5d6s\ ^3D_{2,3}$ , and  $5d6s\ ^1D_2$  transitions, calculated using Eqs. (21) and (22), are listed in rows 2–5, correspondingly. We sum all listed hyperfine quenching rates and present in the last row of the table the branching ratio of this sum to  $W^{(0)}$ .

As we discussed above we consider the results obtained at the CI+all-order+RPA stage as the final (recommended) values as the calculations of other corrections beyond RPA are unreliable for the matrix elements of the  $T^{(k)}$  operators. The

TABLE VIII. The  $6s6p\ ^3P_0^o-5d6s\ ^3D_1$  transition probability,  $W^{(0)}$ , is given in the first row (in  $\text{s}^{-1}$ ). The quenching rates of the  $6s6p\ ^3P_0^o-6s^2\ ^1S_0$ ,  $5d6s\ ^3D_{2,3}$ , and  $5d6s\ ^1D_2$  transitions, obtained in (1) CI+MBPT+RPA, (2) CI+all-order+RPA, and (3) CI+all-order+AC approximations, are listed (in  $\text{s}^{-1}$ ) in rows 2–5, correspondingly. The branching ratios (BR) of the hyperfine quenching rates to  $W^{(0)}$  are presented in the last row. The uncertainties are given in parentheses. The numbers in brackets represent powers of 10.

	(1)	(2)	(3)	Final
$^3P_0^o-^3D_1$	1.69[+7]	1.68[+7]	1.64[+7]	1.68(4)[+7]
$^3P_0^o-^1S_0$	3.55	2.96	2.38	2.96(59)
$^3P_0^o-^3D_2$	3.26	2.96	2.31	2.96(65)
$^3P_0^o-^3D_3$	0.0011	0.0010	0.0008	0.0010(2)
$^3P_0^o-^1D_2$	0.051	0.050	0.041	0.050(9)
BR	4.05[−7]	3.55[−7]	2.88[−7]	3.55(65)[−7]

uncertainties were estimated as the largest difference between the CI+all-order+RPA results and the CI+MBPT+RPA and CI+all-order+AC values.

## V. DISCUSSION

We have measured several key properties of  $^{175}\text{Lu}^+$  that are relevant to practical clock operation with this ion. Hyperfine induced mixing results in a small decay rate out of the detection channel which is dominated by decay into the  $^1S_0$  and  $^3D_2$  levels. This rate provides a fundamental limit to the detection error rate given by  $w/(Wq)$  which is the probability the ion is pumped dark with zero photons detected. For our current collection efficiency this gives a limit of  $1.0 \times 10^{-4}$ . The measured decay rate does not impose any limitations on cooling as most decays are to  $^1S_0$  and  $^3D_2$  which can be quickly repumped.

During clock operation occupation of the  $^1D_2$  level would mostly occur due to repumping to  $^3D_1$ . This occurs with a probability of approximately 2%. In typical clock operation, occupation is split between ground and excited states. So, on average, 1% of the cycles will be compromised provided the cycle time is large enough for the ion to decay from  $^1D_2$  with reasonable probability before the next cycle begins. Occupation of the  $^3D_3$  would result in significant dead time. However, based on the analysis here, these events are infrequent, happening only once every  $1 \times 10^4$  clock cycles. In a multi-ion clock [15] these considerations would only result in a very small number fluctuations such that additional repump lasers would not be necessary.

Calculation of polarizabilities given in Sec. IV A indicate that the differential scalar polarizability,  $\Delta\alpha$ , for the  $^1S_0$  to  $^3D_1$  transition may not be as reported in Ref. [16] and this would have immediate consequences for the proposal given in Ref. [15]. It is therefore essential to obtain an experimental value for this quantity. We have given calculations of  $\Delta\alpha$  at a number of wavelengths that are readily accessible to us. Measurement of  $\Delta\alpha$  at these wavelengths would serve as a useful benchmark for the calculations given here.

Intuitively we can expect  $\Delta\alpha$  to be more negative for the  $^1S_0$ -to- $^3D_2$  transition and we have also given associated calculations for this case. Measurements and calculations

here demonstrate a suitable lifetime for clock operation. Although this transition would be more technically difficult to implement, systematic shifts would be significantly lower than for the  $^1S_0$ -to- $^3D_2$  case. Contributions from the  $^3D_1$  and  $^3D_3$  levels have opposite sign resulting in a partial cancellation of the residual magnetic field shift for the average frequency. Furthermore, due to the reduced lifetime relative to the  $^3D_1$  level, much less intensity is needed to drive the  $^1S_0$ -to- $^3D_2$  transition, resulting in a substantial reduction in the ac Stark shift from the probe beam itself.

### ACKNOWLEDGMENTS

This research is supported by the National Research Foundation, Prime Minister's Office, Singapore and the Ministry of Education, Singapore under the Research Centres of Excellence programme. This work was supported in part by U.S. NSF Grant No. PHY-1520993 and the Australian Research Council.

### APPENDIX: THE HYPERFINE INTERACTION

The hyperfine structure (hfs) coupling due to nuclear multipole moments may be represented as a scalar product of two tensors of rank  $k$ ,

$$H_{\text{hfs}} = \sum_k H_{\text{hfs},k} = \sum_k (\mathbf{N}^{(k)} \cdot \mathbf{T}^{(k)}),$$

where  $\mathbf{N}^{(k)}$  and  $\mathbf{T}^{(k)}$  act in the space of nuclear and electronic coordinates, respectively. Using this expression we write the  $H_{\text{hfs}}$  matrix element as

$$\begin{aligned} & \langle \gamma' I J'; F M_F | H_{\text{hfs}} | \gamma I J; F M_F \rangle \\ &= (-1)^{I+J'+F} \sum_k \langle I || N^{(k)} || I \rangle \langle \gamma' J' || T^{(k)} || \gamma J \rangle \\ & \quad \times \begin{Bmatrix} I & I & k \\ J & J' & F \end{Bmatrix}, \end{aligned}$$

where  $\mathbf{I}$  is the nuclear spin,  $\mathbf{J}$  is the total angular momentum of the electrons,  $\mathbf{F} = \mathbf{J} + \mathbf{I}$ ,  $M_F$  is the projection of the total momentum  $\mathbf{F}$  to the quantization axis, and  $\gamma$  encapsulates all other atomic quantum numbers.

Below, we restrict the treatment of  $H_{\text{hfs}}$  to the first two terms in the sum over  $k$ ; i.e., we consider only the interaction of magnetic dipole and electric quadrupole nuclear moments

with the electrons. Thus,

$$H_{\text{hfs}} \approx \mathbf{N}^{(1)} \cdot \mathbf{T}^{(1)} + \mathbf{N}^{(2)} \cdot \mathbf{T}^{(2)}.$$

It is convenient to express the matrix elements  $\langle I || N^{(1)} || I \rangle$  and  $\langle I || N^{(2)} || I \rangle$  through the nuclear magnetic dipole moment  $\boldsymbol{\mu}$  and nuclear electric quadrupole moment  $Q$ , respectively. They are defined as follows:

$$\begin{aligned} \mu &= \langle I M_I = I | \boldsymbol{\mu}_z | I M_I = I \rangle = \begin{pmatrix} I & 1 & I \\ -I & 0 & I \end{pmatrix} \langle I || \boldsymbol{\mu} || I \rangle \\ &= \sqrt{\frac{I}{(2I+1)(I+1)}} \langle I || \boldsymbol{\mu} || I \rangle, \\ Q &= 2 \langle I M_I = I | Q_0^{(2)} | I M_I = I \rangle \\ &= 2 \begin{pmatrix} I & 2 & I \\ -I & 0 & I \end{pmatrix} \langle I || Q || I \rangle \\ &= 2 \sqrt{\frac{I(2I-1)}{(2I+3)(2I+1)(I+1)}} \langle I || Q || I \rangle. \end{aligned}$$

We define  $\mathbf{N}^{(1)}$  and  $N_q^{(2)}$  in dimensionless form as

$$\begin{aligned} \mathbf{N}^{(1)} &= \boldsymbol{\mu} / \mu_N, \\ N_q^{(2)} &= Q_q^{(2)} / [1 \text{ b}], \end{aligned}$$

where  $\mu_N$  is the nuclear magneton ( $\mu_N = \frac{e\hbar}{2m_p c}$ , with  $m_p$  being the proton mass), and the reduced matrix elements are given by

$$\begin{aligned} \langle I || N^{(1)} || I \rangle &= \sqrt{\frac{(2I+1)(I+1)}{I}} \frac{\mu}{\mu_N}, \\ \langle I || N^{(2)} || I \rangle &= \frac{1}{2} \sqrt{\frac{(2I+3)(2I+1)(I+1)}{I(2I-1)}} \left[ \frac{Q}{1 \text{ b}} \right]. \end{aligned}$$

We define one-particle electronic tensors (in a.u.) as

$$\begin{aligned} T_q^{(1)} &= -\frac{i\alpha\sqrt{2}(\boldsymbol{\gamma}_0 \boldsymbol{\gamma} \cdot \mathbf{C}_{1q}^{(0)}(\hat{\mathbf{r}}))}{r^2} \mu_N, \\ T_q^{(2)} &= -\frac{C_q^{(2)}(\hat{\mathbf{r}})}{r^3} \times [1 \text{ b}]. \end{aligned}$$

Here  $\alpha$  is the fine-structure constant,  $\mathbf{C}_{1q}^{(0)}$  is a normalized spherical harmonic,  $\boldsymbol{\gamma}_0$  and  $\boldsymbol{\gamma}$  are the Dirac matrices, and  $C_q^{(2)}$  is a normalized spherical function.

- 
- [1] T. Rosenband, D. B. Hume, P. O. Schmidt, C. W. Chou, A. Brusch, L. Lorini, W. H. Oskay, R. E. Drullinger, T. M. Fortier, J. E. Stalnaker, S. A. Diddams, W. C. Swann, N. R. Newbury, W. M. Itano, D. J. Wineland, and J. C. Bergquist, *Science* **319**, 1808 (2008).
- [2] X. Zhang, M. Bishof, S. L. Bromley, C. V. Kraus, M. S. Safronova, P. Zoller, A. M. Rey, and J. Ye, *Science* **345**, 1467 (2014).
- [3] M. J. Martin, M. Bishof, M. D. Swallows, X. Zhang, C. Benko, J. von Stecher, A. V. Gorshkov, A. M. Rey, and J. Ye, *Science* **341**, 632 (2013).
- [4] C. W. Chou, D. B. Hume, J. C. J. Koelemeij, D. J. Wineland, and T. Rosenband, *Phys. Rev. Lett.* **104**, 070802 (2010).
- [5] B. J. Bloom, T. L. Nicholson, J. R. Williams, S. L. Campbell, M. Bishof, X. Zhang, W. Zhang, S. L. Bromley, and J. Ye, *Nature (London)* **506**, 71 (2014).
- [6] J. E. Stalnaker, S. Diddams, T. Fortier, K. Kim, L. Hollberg, J. Bergquist, W. Itano, M. Delany, L. Lorini, W. Oskay, T. Heavner, S. Jefferts, F. Levi, T. Parker, and J. Shirley, *Appl. Phys. B* **89**, 167 (2007).
- [7] P. Dube, A. A. Madej, Z. Zhou, and J. E. Bernard, *Phys. Rev. A* **87**, 023806 (2013).

- [8] N. Huntemann, M. Okhapkin, B. Lipphardt, S. Weyers, C. Tamm, and E. Peik, *Phys. Rev. Lett.* **108**, 090801 (2012).
- [9] Y. H. Wang, R. Dumke, T. Liu, A. Stejskal, Y. Zhao, J. Zhang, Z. Lu, L. J. Wang, T. Becker, and H. Walther, *Opt. Commun.* **273**, 526 (2007).
- [10] Z. W. Barber, C. W. Hoyt, C. W. Oates, L. Hollberg, A. V. Taichenachev, and V. I. Yudin, *Phys. Rev. Lett.* **96**, 083002 (2006).
- [11] A. D. Ludlow, M. M. Boyd, J. Ye, E. Peik, and P. Schmidt, *Rev. Mod. Phys.* **87**, 637 (2015).
- [12] N. Hinkley, J. A. Sherman, N. B. Phillips, M. Schioppa, N. D. Lemke, K. Beloy, M. Pizzocaro, C. W. Oates, and A. D. Ludlow, *Science* **341**, 1215 (2013).
- [13] T. L. Nicholson, S. L. Campbell, R. B. Hutson, G. E. Marti, B. J. Bloom, R. L. McNally, W. Zhang, M. D. Barrett, M. S. Safronova, G. Strouse, W. L. Tew, and J. Ye, *Nat. Commun.* **6**, 6896 (2015).
- [14] M. D. Barrett, *New J. Phys.* **17**, 053024 (2015).
- [15] K. Arnold, E. Hajiyev, E. Paez, C. H. Lee, M. D. Barrett, and J. Bollinger, *Phys. Rev. A* **92**, 032108 (2015).
- [16] A. Kozlov, V. A. Dzuba, and V. V. Flambaum, *Phys. Rev. A* **90**, 042505 (2014).
- [17] B. L. Chuah, N. C. Lewty, and M. D. Barrett, *Phys. Rev. A* **84**, 013411 (2011).
- [18] N. C. Lewty, B. L. Chuah, R. Cazan, B. K. Sahoo, and M. D. Barrett, *Opt. Express* **20**, 21379 (2012).
- [19] A. H. Myerson, D. J. Szwer, S. C. Webster, D. T. C. Allcock, M. J. Curtis, G. Imreh, J. A. Sherman, D. N. Stacey, A. M. Steane, and D. M. Lucas, *Phys. Rev. Lett.* **100**, 200502 (2008).
- [20] M. S. Safronova, M. G. Kozlov, W. R. Johnson, and D. Jiang, *Phys. Rev. A* **80**, 012516 (2009).
- [21] V. A. Dzuba, V. V. Flambaum, and M. G. Kozlov, *Phys. Rev. A* **54**, 3948 (1996).
- [22] V. A. Dzuba, M. G. Kozlov, S. G. Porsev, and V. V. Flambaum, *Zh. Eksp. Teor. Fiz.* **114**, 1636 (1998) [*Sov. JETP* **87**, 885 (1998)].
- [23] R. Sternheimer, *Phys. Rev.* **80**, 102 (1950).
- [24] A. Dalgarno and J. T. Lewis, *Proc. R. Soc. London, Ser. A* **233**, 70 (1955).
- [25] M. G. Kozlov and S. G. Porsev, *Eur. Phys. J. D* **5**, 59 (1999).
- [26] Yu. Ralchenko, A. Kramida, J. Reader, and the NIST ASD Team (2011). NIST Atomic Spectra Database (version 4.1), National Institute of Standards and Technology, Gaithersburg, MD. <http://physics.nist.gov/asd>.
- [27] M. S. Safronova, S. G. Porsev, U. I. Safronova, M. G. Kozlov, and C. W. Clark, *Phys. Rev. A* **87**, 012509 (2013).
- [28] T. Brenner, S. Uüttgenbach, W. Rupprecht, and F. Traäher, *Nucl. Phys. A* **440**, 407 (1985).
- [29] P. Pyykkö, *Mol. Phys.* **99**, 1617 (2001).